crystals

MDPI

Article

Multiphysics Analysis of Porous MWCNT Films with Tunable Thermo-Optical, Nonlinear Optical, and Magneto-Optical Responses

José Antonio García-Merino

Departamento de Mecánica, Facultad de Ingeniería, Universidad Tecnológica Metropolitana, Jose Pedro Alessandri 1242, Nuñoa, Santiago 775000, Chile; jgarciam@utem.cl

Abstract

Porous multi-walled carbon nanotube (MWCNT) films combine strong optical absorption with thermal, Kerr-like, thermo-optical, and magneto-optical responses. However, these effects depend on film structure and may require different design conditions. In this work, a multiphysics model was used to analyze 12 MWCNT film configurations with dependance on thicknesses, porosity, and orientation parameters. The model included optical attenuation, transient heating, nonlinear refraction, thermo-optic modulation, magneto-optical response, and optical phase shift under irradiances of 7–20 MW cm^{-2} and magnetic fields up to 1 T. Optical density ranged from approximately 0.4 to 2.8, while transmittance showed negligible variation with irradiance. Thin and porous films produced the highest temperature rises, approximately 4.5 K, and the largest total refractive-index changes. In contrast, thicker films generated larger accumulated phase shifts. The thermo-optic contribution is dominated under nanosecond laser irradiation. As the pulse duration approached the picosecond regime, the lower deposited energy reduced the photothermal response, so the Kerr-like and magneto-optical terms accounted for a larger total refractive-index change. This predictive parametric study identifies architecture- and pulse-dependent trends for future experimental evaluation of multifunctional MWCNT films.

Keywords: multi-walled carbon nanotubes; nonlinear optics; magneto-optical coupling; thermo-optical response

1. Introduction

Carbon nanotube films remain technologically relevant because they combine broadband optical absorption, low density, electrical conductivity, mechanical flexibility, and highly anisotropic thermal transport within a single material architecture. These characteristics have enabled their use as black absorbers, thermal and infrared detectors, transparent or flexible electrodes, electromagnetic shields, photothermal converters, and active elements in electronic and optoelectronic devices [1–7]. Unlike conventional homogeneous coatings, however, the macroscopic properties of MWCNT films are not determined exclusively by the intrinsic behavior of the individual nanotubes [8]. Film thickness, porosity, nanotube connectivity, and orientational order regulate the number and quality of intertube contacts, the available optical interaction length, and the pathways for charge and heat transport [9–12]. Increasing thickness generally enhances optical attenuation and reduces sheet resistance, but also increases the areal thermal capacity. Porosity decreases the effective amount of solid material and modifies photon trapping and heat dissipation, whereas

Check for updates

Academic Editors: Miłosz Grodzicki and Dominika Majchrzak

Received: 15 August 2026
Revised: 27 August 2026
Accepted: 31 August 2026
Published: 2 September 2026

Copyright: © 2026 by the author. Licensee MDPI, Basel, Switzerland. This article is an open access article distributed under the terms and conditions of the Creative Commons Attribution (CC BY) license.

alignment introduces directional dependence into the electrical conductivity, thermal conductivity, and optical absorption relative to the incident polarization [13,14]. Consequently, these structural variables may improve one functional response while simultaneously limiting another.

The architecture of CNT films can be adjusted through several fabrication routes. Their thickness can be controlled by the deposited CNT concentration, the number of coating or transfer cycles, filtration volume, or growth time during chemical vapor deposition [15]. Porosity can be modified through the initial nanotube concentration, growth density, mechanical compression, solvent-induced densification, or the incorporation and subsequent removal of sacrificial phases [16]. Nanotube alignment can be promoted during direct growth or through shear flow, mechanical stretching, controlled vacuum filtration, dielectrophoresis, and external magnetic fields [17,18]. These methods allow the transition from randomly interconnected porous networks to partially or highly aligned architectures. Nevertheless, simultaneously controlling thickness, porosity, and alignment remains challenging because these parameters are not independent in real films. For example, densification reduces porosity but also increases intertube contact and electrical conductivity, while alignment can improve axial heat transport and polarization-dependent absorption without necessarily increasing the optical absorbed energy [19–24]. A systematic parametric analysis is therefore required to separate their individual and combined contributions.

Compared with conventional dark coatings based on metallic blacks, oxides, carbon paints, or polymer–pigment composites, CNT films offer broadband absorption, extremely low reflectance, low areal mass, flexibility, and resistance to electrochemical corrosion [1,11]. Furthermore, their optical absorption can be combined with electrical, thermal, nonlinear-optical, and magnetically tunable responses [25,26]. Their network structure also enables properties that are difficult to obtain simultaneously in ordinary coatings, including polarization-dependent absorption, anisotropic heat conduction, and nonlinear refractive-index modulation. These characteristics linked CNT materials with applications ranging from logic circuits and high-frequency electronics to magnetoresistance devices [27–29]. However, CNT coatings also present important limitations. Pristine nanotubes have low wettability and tend to agglomerate because of strong van der Waals interactions, which complicates dispersion, deposition, and adhesion to many substrates. Surface functionalization, binders, or intermediate layers can improve adhesion and processability, but may alter electronic transport, reduce nanotube–nanotube contact, or introduce additional thermal resistance [30]. Furthermore, although CNT films do not undergo metallic corrosion, they are not immune to oxidation at sufficiently high temperatures in air. Their possible relevance to quantum technologies should therefore be described cautiously: individual CNTs and CNT quantum dots have demonstrated spin transport and quantum confinement, whereas porous MWCNT films are more realistically considered tunable conductive or magneto-optical interfaces for precision electronic and sensing architectures [31,32].

The broad range of properties reported for CNT films further illustrates why thickness, porosity, and alignment must be considered when defining their operating regime. At room temperature, freestanding CNT buckypapers have exhibited in-plane thermal conductivities of approximately 81 W $m^{-1}K^{-1}$ for randomly oriented networks, compared with 153 W $m^{-1}K^{-1}$ parallel and 72 W $m^{-1}K^{-1}$ perpendicular to the preferential nanotube direction, corresponding to a thermal anisotropy ratio of about 2.1 [33]. Their optical behavior can extend from semitransparent to nearly black: CNT networks approximately 100 nm thick can retain visible transmittances close to 88%, whereas films approaching 10 μm can absorb more than 99% of the incident radiation; broadband attenuation has also been demonstrated for random MWCNT films over wavelengths from 300 nm to 400 μm [34–36]. On the other hand, magnetic effects are generally weaker and require com-

paratively stronger external fields. MWCNT thin films have shown magnetically controlled electrical conductivity and nonlinear optical transmission at fields reaching approximately 5 T. In addition, negative magnetoresistance associated with weak localization and inter-tube transport has been investigated between 4.2 and 200 K under fields up to 9 T [25,37]. These values place the present study of 10–30 μm thick films within the strongly absorbing regime, whereas the modeled magnetic-field interval of 0–1 T represents a comparatively low-field operating window. This combination of architectural and operating parameters provides a suitable framework for examining how thermal, nonlinear-optical, and magneto-optical mechanisms interact across different MWCNT film configurations.

Despite extensive research on CNT-based coatings, thickness, porosity, and alignment are commonly examined separately. Consequently, their coupled influence on thermal, electronic nonlinear, thermo-optical, and magneto-optical responses remains insufficiently resolved [38,39]. This limitation is relevant when some intrinsic material coefficients remain almost unchanged, while the observable macroscopic response varies since the film architecture modifies optical absorption, effective transport, thermal storage, and interaction length. This study presents a multiphysics framework for 12 porous MWCNT film configurations, combining three thicknesses (10, 20, and 30 μm), two porosities ($\phi = 0.3$ and 0.4), and two orientational states ($S = 0$ and 0.5). The model connects the structural parameters with effective density, areal heat capacity, optical attenuation, anisotropic thermal transport, temperature rise, nonlinear and thermo-optical refractive-index changes, magneto-optical adjustment, and accumulated optical phase shift. The novelty lies in identifying architecture-dependent trends within the investigated parameter ranges rather than seeking a single universally optimal film. The analysis demonstrates how thin and porous films can favor thermal and refractive index modulation, whereas thicker architectures can enhance the accumulated phase response. This provides a theoretical basis for future experimental evaluation for efficient absorbing MWCNT films according to the required thermo-opto-magnetic functionality.

2. Methodology

2.1. Definition of MWCNT Variants and Material Parameters

To systematically investigate the influence of the film morphology on the thermo-optical response, a parametric numerical study was carried out by varying three key structural parameters of the MWCNT films: thickness, porosity, and nanotube alignment. Film thicknesses of 10, 20, and 30 μm were selected to represent the typical range reported for free-standing carbon nanotube films. Two porosity levels (0.3 and 0.4) were considered to account for differences in packing density resulting from the fabrication process, while two alignment states were analyzed: 0, corresponding to randomly oriented nanotubes, and 1/2, representing partially aligned nanotubes along a preferred direction. The combination of these variables generated a total of 12 different film configurations, allowing the individual and coupled effects of each structural parameter on the optical, thermal, and thermo-optical behavior to be evaluated.

The material properties employed in the numerical simulations are summarized in Table 1. The thermophysical, mechanical, and optical parameters were selected from representative values reported in the literature for MWCNT films and were assumed to remain constant throughout the simulations. In contrast, the film thickness, porosity, and nanotube alignment were treated as independent variables in the parametric study. Two porosity values, $\phi = 0.3$ and 0.4, were selected based on an experimental value of approximately 0.36 reported for CNT films [40]. This range was used to evaluate how small changes in porosity affect the film response while keeping the other material properties constant. These values represent the conditions analyzed in the model and not general

limits for MWCNT films. The thickness range of 10–30 μm was selected based on CNT films grown by CVD using bilayer metallic catalyst systems, which allow controlled CNT nucleation and film thickness within this range [41]. This approach allows the influence of the film microstructure on the thermal transport, optical absorption, and thermo-optical response to be isolated while maintaining identical intrinsic material properties for all simulated configurations. Moreover, in the absence of a directly reported Cotton–Mouton coefficient for porous MWCNT films, C_B was treated as a phenomenological parameter rather than as an experimentally established material property. Previous measurements on MWCNT films showed nonlinear trends in optical properties as a function of magnetic field, which were modeled using a second-order susceptibility [25]. These experimental results support the phenomenological quadratic field dependence adopted in the present model, although the selected value of $C_B = 1.0 \times 10^{-4}\mathrm{T}^{-2}$ remains a nominal modeling parameter.

Table 1. Thermophysical, magnetic, and optical properties of the MWCNT film employed in the numerical simulations.

Property	Symbol	Value	Unit	Reference
Density	ρ	1340	$kg{\cdot}m^{-3}$	[42]
Thermal conductivity	k	70	$W{\cdot}m^{-1}{\cdot}K^{-1}$	[40]
Specific heat capacity	C_p	2100	$J{\cdot}kg^{-1}{\cdot}K^{-1}$	[40]
Linear refractive index	n_0	1.55	–	[24]
Nonlinear refractive index	n_2	-1.0×10^{-11}	$cm^2\ W^{-1}$	[24]
Nonlinear absorption coefficient	β	-3.5×10^{-8}	$cm\ W^{-1}$	[24]
Linear absorption coefficient	α_0	4600	cm^{-1}	[24]
Thermo-optic coefficient	dn/dT	-5.0×10^{-3}	$^{\circ}C^{-1}$	[26]
Magneto-optical coefficient	C_B	1.0×10^{-4}	T^{-2}	–

The thermophysical and optical parameters used in the simulations were selected from representative values reported in the literature. However, their combined use for porous MWCNT films with the specific thicknesses, porosities, and alignment states considered here has not yet been validated against corresponding experimental measurements. Therefore, the present work should be regarded as a predictive parametric study aimed at identifying relative trends among film architecture. The absolute values depend on the assumed material properties, effective-medium relations, and boundary conditions, and should be verified experimentally using films tested under equivalent optical and magnetic conditions.

2.2. Properties Calculations for MWCNT Film Configurations

The porous MWCNT films were characterized by three structural parameters: thickness h, porosity ϕ, and nanotube alignment parameter S. The intrinsic thermophysical properties of the MWCNT material were maintained unchanged across all configurations. Therefore, the differences among the modeled films arise from changes in their architecture rather than from the arbitrary assignment of different material properties. Porosity determines the solid fraction contained within the film, thickness controls the amount of material and thermal storage per unit area, and alignment modifies the coupling between the linearly polarized laser field and the nanotube network.

Neglecting the comparatively small mass and heat capacity of the air contained within the pores, the effective density of the porous film was calculated using a volume-averaging approximation, $\rho_{\mathrm{eff}} = (1-\phi)\rho_{\mathrm{MWCNT}}$, where ρ_{MWCNT} is the density of the

compact MWCNT material [40]. The mass per unit area of each film was subsequently obtained as:

$$\frac{m}{A} = \rho_{\text{eff}} h = (1 - \phi)\rho_{\text{MWCNT}} h \quad (1)$$

where m is the film mass and A is its surface area. Equation (1) shows that increasing either porosity or decreasing thickness reduces the amount of solid material interacting with the incident radiation. The effective volumetric heat capacity was determined from: $C_{\text{vol}} = \rho_{\text{eff}} C_p$, where C_p is the intrinsic specific heat capacity of the MWCNTs. Since the incident laser energy and heat source are expressed per unit surface area, the thermal storage capacity of the films was represented by the areal heat capacity:

$$C_A = C_{\text{vol}} h = (1 - \phi)\rho_{\text{MWCNT}} C_p h \quad (2)$$

Thus, thickness does not modify the volumetric heat capacity but directly increases the areal heat capacity. Conversely, increasing porosity reduces both quantities because of the lower effective density. The calculated values for all film configurations are summarized in Table 2.

Table 2. Calculated properties for the 12 MWCNT film configurations.

Conf.	h (μm)	ϕ	S	ρ_{eff} (kg m^{-3})	m/A (kg m^{-2})	C_{vol} (MJ m^{-3}K^{-1})	C_A (J m^{-2} K^{-1})	η(S)
F1	10	0.3	0	938.0	0.00938	1.9698	19.70	1/3
F2	10	0.3	½	938.0	0.00938	1.9698	19.70	2/3
F3	10	0.4	0	804.0	0.00804	1.6884	16.88	1/3
F4	10	0.4	½	804.0	0.00804	1.6884	16.88	2/3
F5	20	0.3	0	938.0	0.01876	1.9698	39.40	1/3
F6	20	0.3	½	938.0	0.01876	1.9698	39.40	2/3
F7	20	0.4	0	804.0	0.01608	1.6884	33.77	1/3
F8	20	0.4	½	804.0	0.01608	1.6884	33.77	2/3
F9	30	0.3	0	938.0	0.02814	1.9698	59.09	1/3
F10	30	0.3	½	938.0	0.02814	1.9698	59.09	2/3
F11	30	0.4	0	804.0	0.02412	1.6884	50.65	1/3
F12	30	0.4	½	804.0	0.02412	1.6884	50.65	2/3

Additionally, the interaction between the linearly polarized laser field and the nanotube network was described through the orientation Hermans factor as [43]:

$$\eta(S) = \frac{1 + 2S}{3} \quad (3)$$

where S is the orientational order parameter. In this work, $S = 0$ represents a randomly oriented nanotube network, whereas $S = 1/2$ describes partial alignment along the direction of the incident electric-field polarization. These values result in $\eta(0) = 1/3$, and $\eta(1/2) = 2/3$. The factor $\eta(S)$ represents the ensemble-averaged projection of the nanotube axes onto the laser polarization direction. Finally, Table 2 summarizes the 12 film configurations obtained by combining three thicknesses, two porosities, and two nanotube orientation states. It also presents the resulting structural and thermal properties used to evaluate their multifunctional response.

2.3. Theoretical Description of Thermal, Optical, and Magneto-Optical Effects

The interaction between the incident laser radiation and the porous MWCNT films was described using a sequential multiphysics model. First, film porosity and nanotube alignment determine the effective optical absorption. The absorbed optical energy sub-

sequently produces a transient temperature field, which modifies the refractive index through the thermo-optic effect. Simultaneously, the incident irradiance produces an electronic nonlinear contribution, whereas the external magnetic field introduces an additional magneto-optical variation. The total refractive-index change and accumulated optical phase shift were obtained by combining these contributions.

2.3.1. Linear and Nonlinear Optical Absorption

The optical response of the MWCNT films was modeled by considering both linear and irradiance-dependent absorption. The nonlinear variation of the absorption coefficient was calculated as:

$$\Delta\alpha_{\mathrm{NL}}(I) = \beta I \tag{4}$$

where I is the incident irradiance and β is the nonlinear absorption coefficient. The irradiance-dependent absorption coefficient of the MWCNT material was therefore expressed as:

$$\alpha(I) = \alpha_0 + \Delta\alpha_{\mathrm{NL}}(I) = \alpha_0 + \beta I \tag{5}$$

where α_0 is the linear absorption coefficient. In the present model, $\beta < 0$, indicating that the effective absorption decreases as the incident irradiance increases, consistently with an effective saturable-absorption-type response within the investigated irradiance interval. The transmittance of a beam in this nonlinear regime can be expressed as:

$$T = \frac{\exp(-h\alpha(I))}{1 + h\beta I} \tag{6}$$

The effects of porosity and nanotube orientation were incorporated through the solid fraction $(1 - \phi)$ and the optical coupling factor $\eta(S)$, respectively. The effective absorption coefficient of each film configuration was therefore calculated as:

$$\alpha_{\mathrm{eff}}(I, \phi, S) = (1 - \phi)\eta(S)(\alpha_0 + \beta I) \tag{7}$$

Equations (4)–(7) describe the combined influence of the electronic nonlinear absorption, porosity, alignment, and film thickness. Assuming negligible optical reflection, the effective absorptance of each film configuration was calculated as $A_{eff}(I, \phi, S, h) = 1 - \mathrm{T}$, where A_{eff} is the fraction of the incident optical power absorbed by the film. This expression accounts for the exponential attenuation of the optical intensity through the film thickness. The effective absorptance was subsequently used to calculate the heat source produced by each film configuration. Since the irradiance-dependent coefficient in Equation (4) was evaluated using the incident irradiance, the model assumes that α_{eff} remains uniform through the film thickness.

2.3.2. Laser-Induced Thermal Response

The transient temperature distribution was calculated by treating the MWCNT film as a thermally thin layer. Under this approximation, the temperature is considered approximately uniform across the film thickness but can vary over the in-plane coordinates x and y. The governing two-dimensional heat-transfer equation was expressed as [42]:

$$C_A \frac{\partial \Delta T}{\partial t} = \nabla \cdot [k_{\mathrm{eff}}(\phi, S) h \nabla \Delta T] + q_{abs}(x, y, t) - H_{\mathrm{loss}} \Delta T \tag{8}$$

where $\Delta T(x, y, t) = T(x, y, t) - T_0$, T_0 is the initial ambient temperature, $k_{\mathrm{eff}}(\phi, S)$ is the configuration-dependent in-plane thermal conductivity, and H_{loss} is an effective heat-transfer coefficient accounting for heat exchange with the substrate and surroundings. Equation (8) was solved numerically over an 8×8 mm^2 surface using a two-dimensional

finite-difference method. The initial condition was $\Delta T(x, y, 0) = 0$, while the film boundaries were maintained at ambient temperature.

The absorbed heat flux was represented with a spatial gaussian beam as:

$$q_{abs}(r,t) = \frac{2P_{\text{inc}}A_{eff}}{\pi w_0^2}\exp\left(-\frac{2r^2}{w_0^2}\right)g_{\text{th}}(t) \quad (9)$$

where $r^2 = x^2 + y^2$, P_{inc} is the incident optical power, w_0 is the laser-beam radius, and $g_{\text{th}}(t)$ is the temporal activation function. The latter was set equal to unity during laser irradiation (t_{laser}) and zero after the laser was switched off. Therefore, the absorbed power was not prescribed as identical for all films but varied according to irradiance, thickness, porosity, and nanotube alignment. This formulation allows the optical response of each film configuration to determine its corresponding thermal source. The optical excitation and thermal simulation conditions used in Equations (8) and (9) are summarized in Table 3. The irradiation time corresponds to the total exposure to a 10 Hz pulse train and not to the duration of an individual laser pulse.

Table 3. Optical excitation and thermal simulation conditions.

Parameter	Symbol	Value	Unit
Laser wavelength (nm)	λ	532	nm
Pulsed irradiance	I_{peak}	7–20	$MW{\cdot}cm^{-2}$
Pulse duration	τ_p	4	ns
Repetition rate	f_{rep}	10	Hz
Beam waist	ω_0	0.6	mm
Average incident power	P_{inc}	1.58–4.52	mW
Total irradiation time	t_{laser}	10	s
Heat-loss coefficient	H_{loss}	22	$W{\cdot}m^{-2}{\cdot}K^{-1}$

Although the optical intensity decreases through the film thickness, the 2D optical source was obtained by integrating the Beer–Lambert absorption by preserving the total absorbed power. To evaluate the mean approximation, the film thickness was divided into thin layers, and the local intensity was calculated as $I(z + \Delta z) = I(z)\exp[-\alpha_{\text{eff}}(I(z))\Delta z]$, using $\alpha_{\text{eff}}(I(z)) = (1 - \phi)\eta(S)[\alpha_0 + \beta I(z)]$. The resulting depth-dependent transmittance and absorptance were compared with those calculated using the incident irradiance in α_{eff}. Across all configurations and irradiances, the maximum relative deviations, calculated as $|\,(T, A)_{\text{local}} - (T, A)_{\text{uniform}}\,|/(T, A)_{\text{local}} \times 100$, were 0.083% for transmittance and 0.0033% for absorptance. Moreover, the through-thickness thermal-diffusion time ranged from 5.4×10^{-6} to 7.2×10^{-5} s, much shorter than the 0.1 s interval between pulses and the 10 s irradiation time. Therefore, the averaged approximations considered in the model are valid within the investigated parameter ranges since negligible relative deviations are obtained.

2.3.3. Electronic Nonlinear and Thermo-Optic Contributions

The instantaneous electronic nonlinear response was described using a Kerr-like relation. To account for the amount of optically active material and its orientational coupling with the incident polarization, the effective nonlinear refractive-index change was calculated as:

$$\Delta n_{\text{NL}} = (1 - \phi)\eta(S)n_2 I \quad (10)$$

where n_2 is the nonlinear refractive-index coefficient. Unlike the thermal contribution, this nonlinear response follows the temporal scale of the incident optical excitation. The laser-

induced temperature increase produces an additional refractive-index variation through the thermo-optic effect:

$$\Delta n_T = \frac{dn}{dT}\Delta T_{\max} \tag{11}$$

where dn/dT is the thermo-optic coefficient and $\Delta T_{\max}$ is obtained from the thermal model.

2.3.4. Magneto-Optical Contribution

For the transverse magnetic-field geometry considered in the simulations, the magnetically induced refractive-index change was represented using a quadratic Cotton–Mouton-type relation [44]:

$$\Delta n_B = C_B(1-\phi)\eta(S)B^2 \tag{12}$$

where C_B is the effective magneto-optical coefficient and B is the magnetic flux density. Equation (12) is an effective low-order description of the magnetic response and does not imply a substantial physical realignment of the nanotubes during the application of the field. Instead, it represents the comparatively small change in the optical response associated with the magnetically perturbed electronic structure of the MWCNT network.

2.3.5. Total Refractive-Index and Optical Phase Modulation

The total change in refractive index was calculated by adding the electronic nonlinear, thermo-optic, and magneto-optical contributions:

$$\Delta n_{\text{total}} = \Delta n_{\text{NL}} + \Delta n_T + \Delta n_B \tag{13}$$

Accordingly, the refractive index of the film under simultaneous optical, thermal, and magnetic excitation was expressed as $n_{\text{film}} = n_{\text{eff}} + \Delta n_{\text{total}}$, where n_{eff} is the unperturbed effective refractive index of the porous MWCNT film. Finally, the optical phase shift accumulated relative to the basal film was calculated as:

$$\Delta\Phi = \frac{2\pi h}{\lambda}\Delta n_{\text{total}} \tag{14}$$

where λ is the optical wavelength.

2.4. Scheme of Multiphysics Interactions

Figure 1 illustrates the multiphysics framework considered for the MWCNT films. A linearly polarized laser beam propagates normally to the film surface, where part of the incident radiation is absorbed by the nanotube network and the remaining fraction is transmitted. Simultaneously, an external magnetic field is applied perpendicular to the film plane. The two panels compare randomly oriented (S = 0) and partially aligned (S = 1/2) CNT networks for films with different thicknesses and porosities. These structural variables regulate complementary aspects of the response: thickness determines the thermal mass and optical interaction length, porosity modifies the amount of active MWCNT material per unit volume, and nanotube alignment controls the coupling between the incident polarization and the nanotube axes. Consequently, their combined variation governs optical absorption, heat accumulation and redistribution, and the electronic, thermo-optical, and magneto-optical contributions to the total refractive index change. The optical irradiance was varied from 7 to 20 MW cm^{-2}, whereas the applied magnetic field ranged from 0 to 1 T.

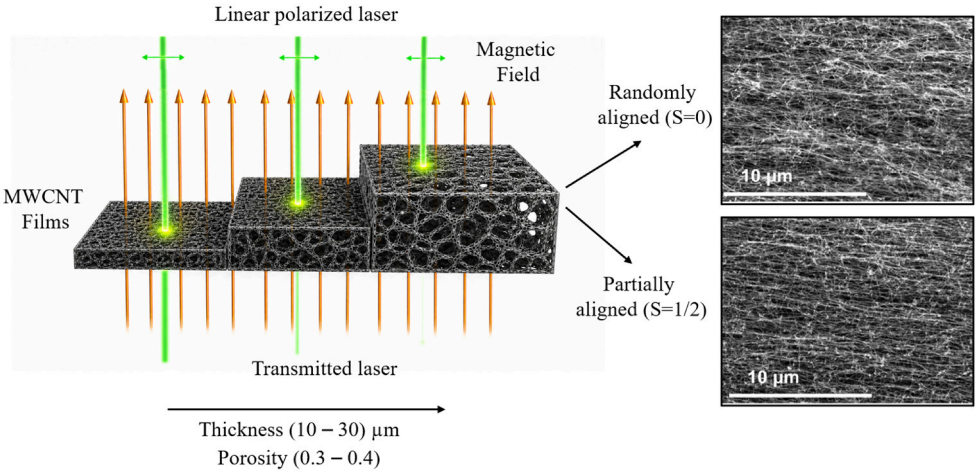


Figure 1. Schematic representation of porous MWCNT films with increasing thickness under linearly polarized laser irradiation and an external magnetic field in randomly oriented and partially aligned nanotube networks. SEM images adapted from ref. [43].

3. Results and Discussion

Figure 2 shows the variation in optical density as a function of film thickness, porosity, and nanotube alignment. Optical density increases linearly with thickness for all configurations. At a fixed thickness and porosity, the partially aligned networks exhibit approximately twice the optical density of the randomly oriented networks, owing to their larger orientation factor. Conversely, increasing the porosity from 0.3 to 0.4 reduces the optical density by approximately 14%, because the fraction of optically active MWCNT material decreases. Consequently, the optical density varies from approximately 0.4 for the thinnest, most porous, randomly oriented F3 film ($h = 10$ μm, $\phi = 0.4$, and $S = 0$) to 2.8 for F10 film ($h = 30$ μm, $\phi = 0.3$, and $S = 1/2$). In summary, thickness produces the largest variation in optical density, while nanotube alignment provides an additional twofold increase.

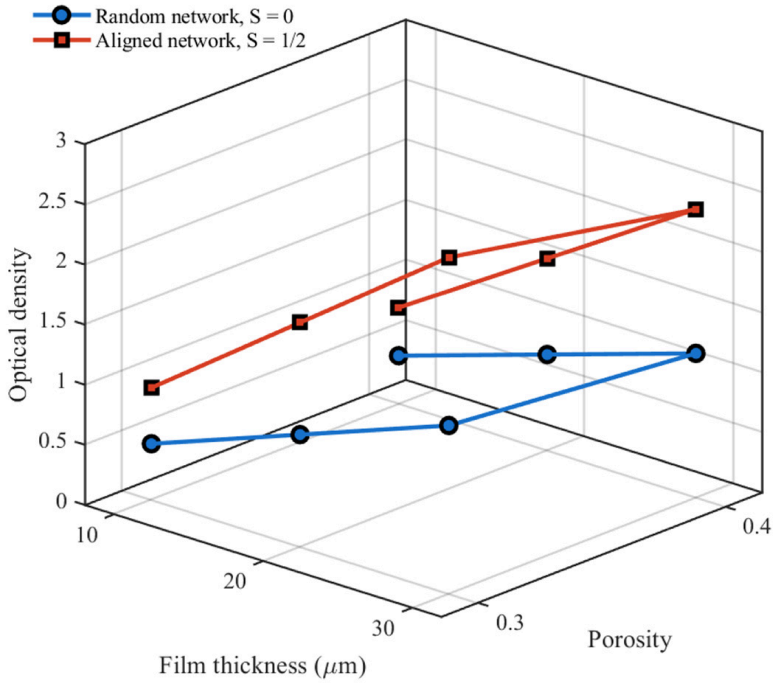


Figure 2. Parametric design and effective film properties.

Figure 3 shows the optical transmittance as a function of incident irradiance for the three film thicknesses. For all configurations, transmittance remains nearly constant throughout the analyzed irradiance range, indicating that the nonlinear modulation is negligible under these conditions. However, film architecture produces substantially larger variations. At h = 10 μm, the randomly oriented networks exhibit the highest transmittance, increasing from approximately 7.7 for ϕ = 0.3 and 11.2% for ϕ = 0.4. Partial nanotube alignment markedly enhances the interaction with the incident polarization, reducing transmittance to approximately 0.6 and 1.3% for ϕ = 0.3 and 0.4, respectively. Increasing the thickness to 20 and 30 μm further suppresses optical transmission because of the longer propagation length and the resulting increase in accumulated absorption. At h = 20 μm, the transmittance of the randomly oriented networks decreases to approximately 0.60 and 1.25% for ϕ = 0.3 and 0.4, respectively, while the partially aligned films show values close to zero. For the 30 μm films, transmittance remains below approximately 0.14% for the randomly oriented networks and approaches zero for the partially aligned configurations. At every thickness, increasing porosity from 0.3 to 0.4 increases transmittance because the fraction of optically active MWCNT material decreases. Overall, thickness and nanotube alignment dominate the transmission response, whereas incident irradiance has no appreciable influence within the analyzed range.

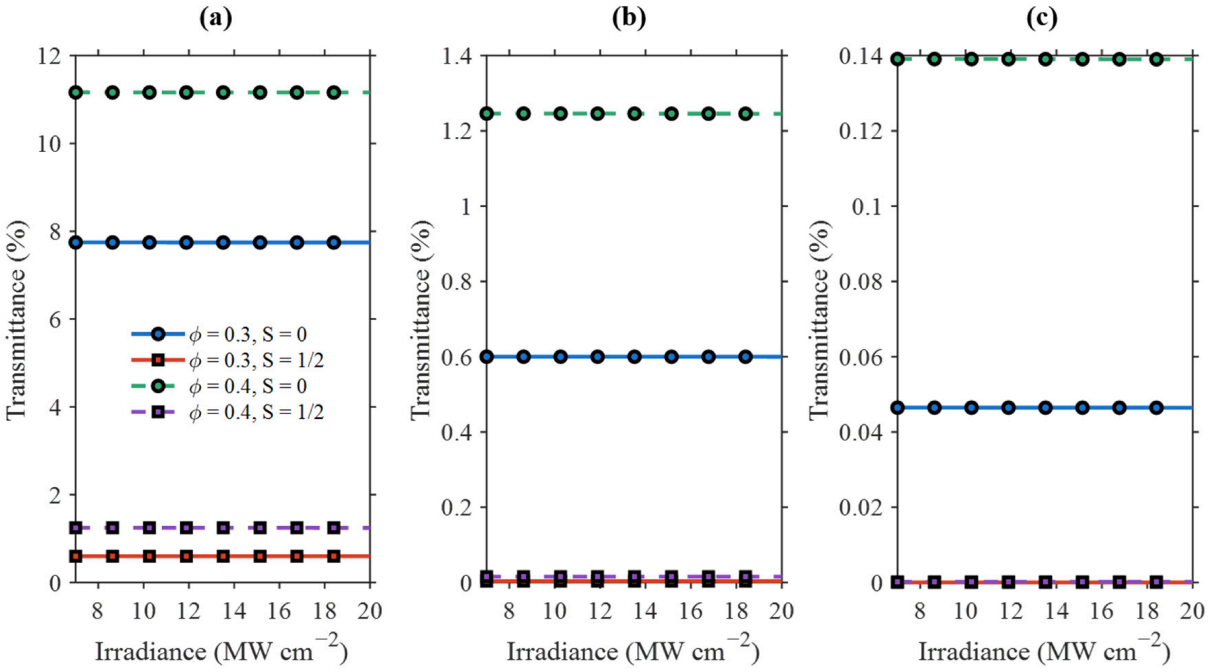


Figure 3. Optical transmittance as a function of irradiance for MWCNT films with thicknesses of (**a**) 10 μm, (**b**) 20 μm, and (**c**) 30 μm, considering porosities of 0.3 and 0.4 and nanotube alignment states of S = 0 and S = 1/2.

Figure 4 presents the simulated laser-induced thermal response of three representative partially aligned MWCNT films with low, intermediate, and high areal heat capacities under a peak irradiance of 20 MW cm^{-2}. The simulations were performed using S = 1/2 and its effective absorption coefficient to determine the absorbed average power. Figure 4a shows the 10 μm film with $\phi = 0.4$, which has the lowest areal heat capacity ($C_A = 16.88$ Jm^{-2}K^{-1}). Its effective absorptance is 0.841, and it reaches the highest maximum temperature rise of approximately 4.5 K. Figure 4b corresponds to heat map of the 20 μm film with $\phi = 0.4$. Increasing the thickness doubles the areal heat capacity to 33.77 J m^{-2} K^{-1} and increases the effective absorptance to 0.975; nevertheless, the maximum temperature rise decreases to

approximately 2.7 K. Figure 4c presents the 30 µm film with $\phi = 0.3$, which has the highest areal heat capacity ($C_A = 59.09$ Jm^{-2}K^{-1}) and an effective absorptance of 0.998. Despite absorbing nearly all the incident optical power, this configuration exhibits the lowest maximum temperature rise, approximately 1.6 K. In all three temperature maps, the Gaussian heat source produces a localized hot spot centered on the irradiation region. Figure 4d compares the temporal evolution of the maximum temperature rise. All configurations exhibit rapid initial heating followed by a quasi-steady regime during irradiation and rapid cooling after the laser is switched off at $t = 10$ s. Although the effective absorptance increases with film thickness, the higher areal heat capacity and greater lateral heat transfer reduce the resulting temperature rise.

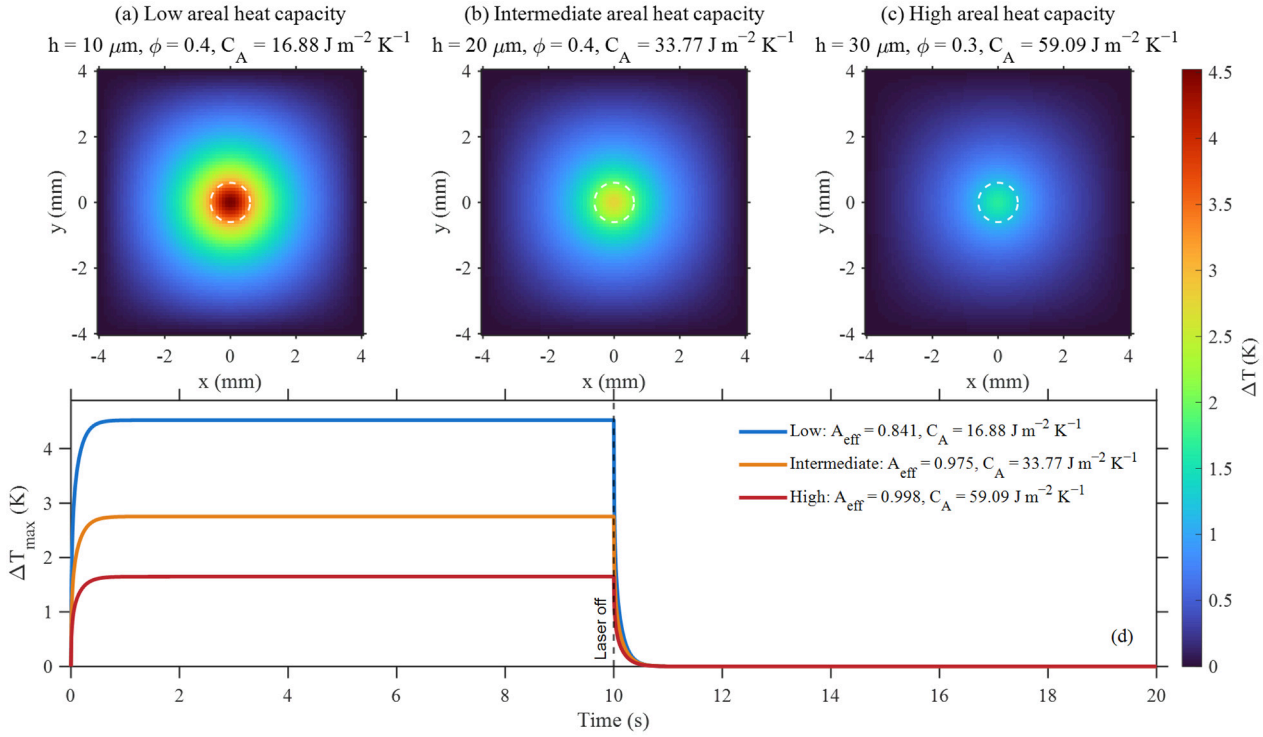


Figure 4. Laser-induced thermal response of representative MWCNT films. Steady-state temperature distributions at 20 MW cm^{-2} for configurations with (**a**) low, (**b**) intermediate, and (**c**) high areal heat capacity. (**d**) Temporal evolution of the maximum temperature rise during 10 s of laser irradiation and the subsequent cooling stage. The dashed circle indicates the laser beam dimensions.

Figure 5 summarizes the influence of film architecture on the simulated thermal response under the same incident irradiance, beam radius, irradiation time, film dimensions, and heat-loss conditions. For each configuration, the absorbed power was calculated from its irradiance-dependent effective absorption coefficient, film thickness, porosity, and nanotube alignment. Thus, the thermal response reflects the combined effects of optical absorption, thermal storage, and lateral heat transport. In Figure 5a, thickness was varied, while the results were averaged over both porosities and alignment states. The decrease in ΔT_{max} with thickness is associated with the greater areal heat capacity and lateral thermal conductance of thicker films. In Figure 5b, porosity was varied while thickness and alignment were averaged over their respective values. Increasing porosity produces a rise in ΔT_{max} because it reduces both the effective thermal mass and heat-spreading capability of the film. In Figure 5c, alignment was varied while thickness and porosity were averaged. The lower ΔT_{max} obtained for $S = 1/2$ indicates that nanotube alignment enhances in-plane heat transport and reduces thermal localization around the irradiated zone. Figure 5d

shows τ_{th} as a function of C_A, where τ_{th} is the thermal response time required for the film to reach thermally stable state under a change in the irradiation conditions. Each curve maintains a fixed combination of porosity and alignment, while thickness varies from 10 to 30 µm. The increase in τ_{th} with C_A indicates a slower thermal response for films with greater thermal mass, whereas nanotube alignment reduces the characteristic time by improving lateral heat diffusion. Overall, thickness mainly controls thermal storage, while porosity and alignment regulate the balance between heat accumulation and redistribution, providing a practical route for tuning the photothermal response of MWCNT films.

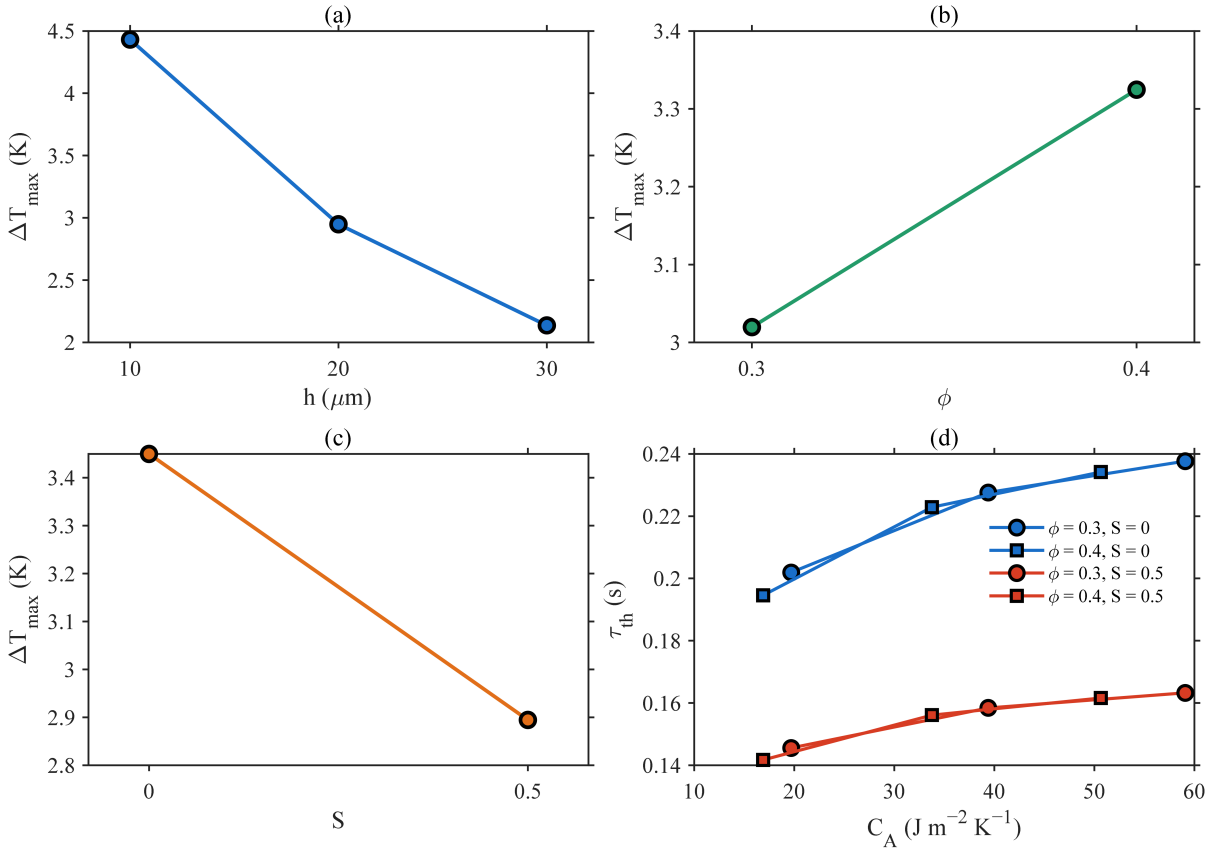


Figure 5. Influence of MWCNT film architecture on the simulated thermal response. Mean ΔT_{max} as a function of (**a**) thickness, (**b**) porosity, and (**c**) nanotube alignment, averaged over the remaining parameters. (**d**) Characteristic thermal time versus areal heat capacity for fixed combinations of ϕ and S, with thickness varying from 10 to 30 µm. All irradiation and boundary conditions were kept constant.

Figure 6 separates the contributions governing the effective refractive-index variation of the MWCNT films. Figure 6a presents the electronic nonlinear contribution, Δn_{NL}, which becomes progressively more negative as the irradiance increases from 7 to 20 MW cm^{-2}. The curves corresponding to different thicknesses overlap because this contribution is governed mainly by porosity and nanotube alignment and is independent of thickness. Aligned films exhibit the largest response, particularly for $\phi = 0.3$, reaching approximately -1.0×10^{-4}. Figure 6b shows the thermo-optic contribution, Δn_T, which also decreases with irradiance but displays a stronger dependence on film thickness. The largest magnitude is obtained for F3 configuration, -0.022 at 20 MW cm^{-2}. This behavior is mainly associated with its low areal heat capacity and reduced lateral heat spreading. F4 exhibits a closely comparable response because its stronger optical coupling is partly balanced by its higher in-plane thermal conductivity.

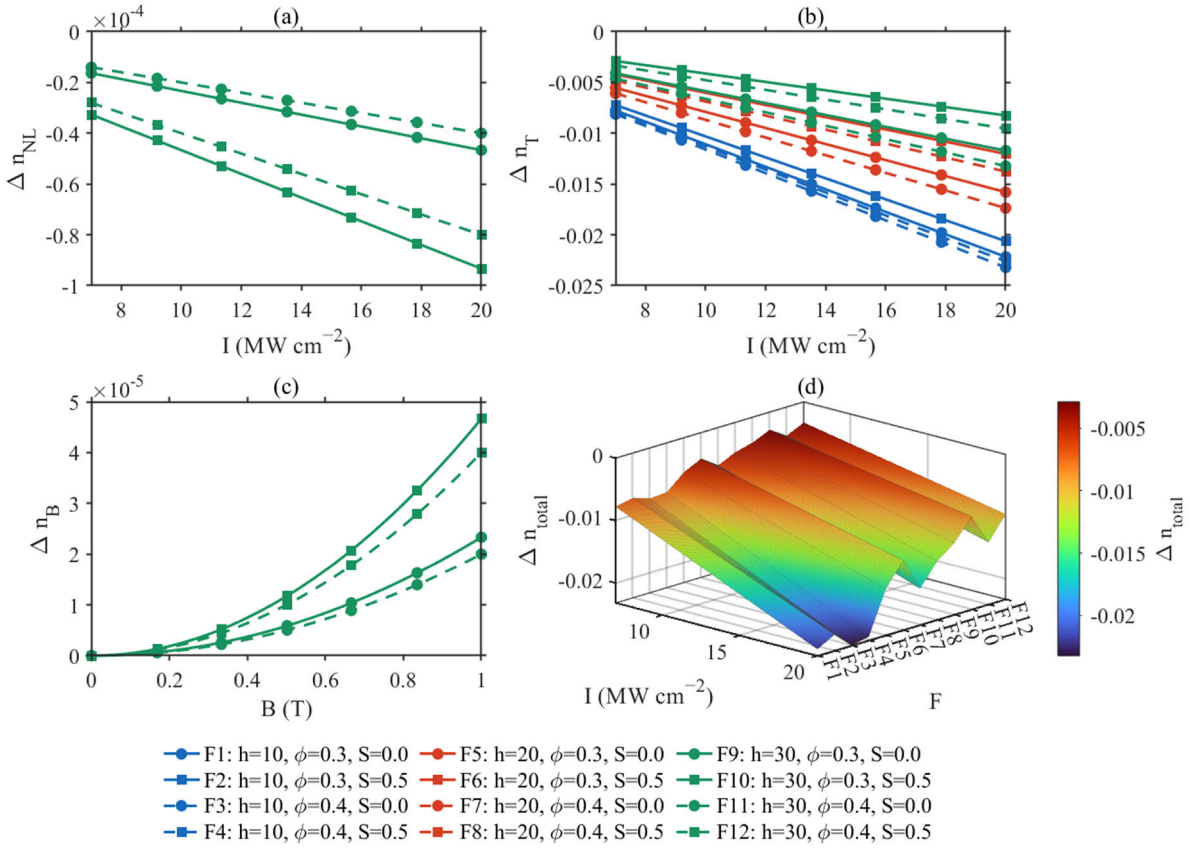


Figure 6. Simulated refractive-index contributions of the 12 MWCNT film configurations: (**a**) electronic nonlinear contribution as a function of optical irradiance, (**b**) thermo-optic contribution as a function of optical irradiance, (**c**) magneto-optical contribution as a function of the applied magnetic field, and (**d**) total refractive-index change as a function of optical irradiance and film configuration.

Figure 6c presents the magneto-optical contribution, Δn_B, as a function of the applied magnetic field. Unlike the electronic and thermal components, this contribution exhibits a nonlinear dependence on B. Its magnitude is enhanced by nanotube alignment and reduced porosity, reaching approximately 5.0×10^{-5} for the aligned configurations with $\phi = 0.3$ at $B = 1$ T. Finally, Figure 6d combines the three contributions and displays the total refractive-index variation, Δn_{total}, for the 12 film configurations in the irradiance range. The total response remains negative since the electronic and, particularly, thermo-optic contributions exceed the positive magneto-optical term. F3 and F4 exhibit the largest absolute variation, with -0.0232 and -0.0226, respectively. Whereas thicker and randomly oriented configurations show considerably weaker modulation. In general, the results indicate that the thermo-optic response dominates the total change in refractive-index, while the electronic and magneto-optical terms provide smaller architecture-dependent corrections.

MWCNT-based films have been extensively investigated because of their outstanding thermal, optical, electrical, and magnetic properties. However, most studies examine these responses individually or under a limited set of structural conditions, providing an incomplete panorama of how multiple properties emerge and interact when several variables are modified simultaneously. In practice, changing film thickness, porosity, or nanotube alignment can enhance one response while attenuating another, producing trade-offs that cannot be identified through single-property optimization. A global analysis is therefore required to establish the sequence of relationships connecting film architecture, optical absorption, heat generation, refractive-index modulation, and accumulated phase shift. Within this framework, Figure 7 integrates the principal responses of the 12 configurations,

allowing their combined behavior to be examined and the most suitable film architecture to be identified according to the intended optical function.

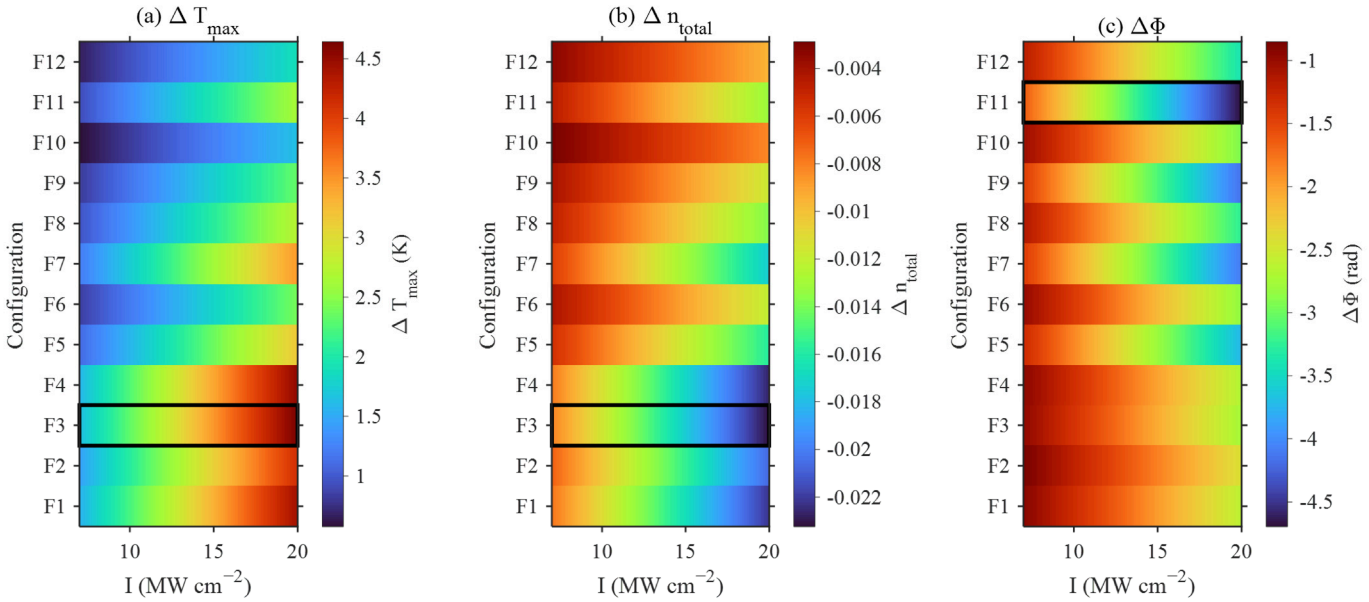


Figure 7. Comparative response of the 12 MWCNT film configurations: (**a**) maximum temperature rise, (**b**) total refractive-index change, and (**c**) accumulated optical phase shift. Panels (**b**,**c**) were calculated at $B = 1$ T.

Figure 7a shows that ΔT_{max} increases with irradiance for all configurations. F3 ($h = 10$ µm, $\phi = 0.4$, and $S = 0$) and F4 ($h = 10$ µm, $\phi = 0.4$, and $S = 0.5$) exhibit the highest and closely comparable temperature rises because they have the lowest areal heat capacity. The stronger optical coupling in F4 is partly balanced by its greater in-plane heat transport, causing F3 to reach a slightly higher temperature. Accordingly, Figure 7b shows that F3 produces a slightly larger $|\Delta n_{total}|$, mainly due to the dominant negative thermo-optic contribution. The electronic Kerr-like term reinforces this effect, whereas the positive magneto-optical component partially compensates it. In Figure 7c, F11 ($h = 30$ µm, $\phi = 0.4$, and $S = 0$) produces the largest phase-shift magnitude because its greater thickness increases the optical interaction length. Thus, thin and porous films favor temperature and refractive-index modulation, whereas thicker films favor accumulated phase modulation.

Even though no single configuration maximizes all the optical responses, the relative importance of the individual mechanisms also depends on the temporal conditions of the optical excitation. Under nanosecond irradiation, heat accumulation produces a dominant thermo-optic effect, while magneto-optical term remains smaller and become negligible. As the pulse duration decreases at fixed peak irradiance and repetition rate, less optical energy is deposited per pulse, reducing the average absorbed power and the resulting temperature rise. The magneto-optical contribution does not increase at shorter pulse durations; rather, it becomes relatively more significant as the thermo-optic term decreases. To examine this effect, Figure 8 presents a pulse-duration plot analysis for F3 configuration over the range from 1 ps to 4 ns, maintaining a peak irradiance of 20 MW cm^{-2}, a repetition rate of 10 Hz, and a total exposure time of 10 s. Figure 8a shows the maximum temperature rise, while Figure 8b compares the magnitudes of the thermo-optic, electronic Kerr-like, magneto-optical, and total refractive-index changes. The results show that ΔT_{max} and the thermo-optic contribution increase in proportion to the pulse duration. Consequently, at picosecond durations the total refractive-index change is mainly determined by the partial compensation between the negative Kerr-like and positive magneto-optical terms, whereas

toward the nanosecond regime the thermo-optic contribution becomes dominant and governs the total response. This analysis describes the accumulated response of the pulse train and does not resolve the ultrafast temperature dynamics within an individual pulse.

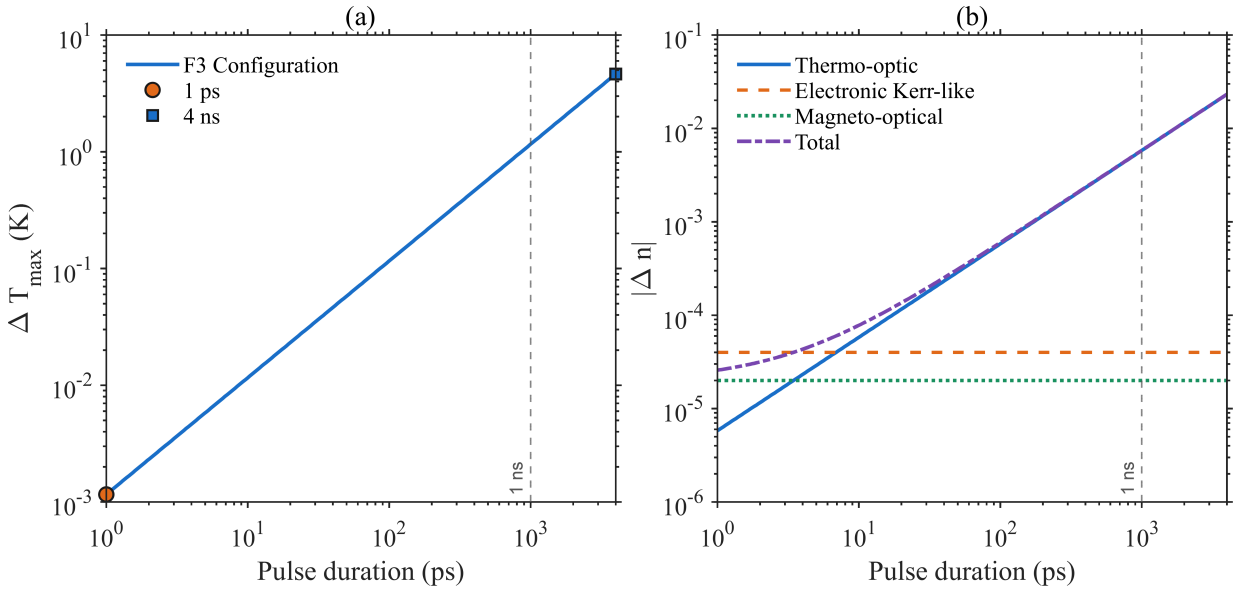


Figure 8. Pulse-duration dependent effect of F3 from 1 ps to 4 ns: (**a**) maximum temperature rise and (**b**) change in refractive index magnitudes. Calculations were performed at 20 MW cm^{-2}, 10 Hz, and B = 1 T.

Beyond the pulse-duration range explored in Figure 8, the response of MWCNT films may also depend on the excitation wavelength, pore morphology, structural defects, and components introduced during synthesis and processing. The present predictions are restricted to 532 nm, while experimental studies show that the transmittance of MWCNT networks varies with wavelength and generally increases toward the near-infrared region [35]. Therefore, if the effective absorption coefficient is lower at 1064 nm, the optical penetration depth would increase, but the absorbed power and temperature rise could decrease. For the same refractive-index change and film thickness, the relation $\Delta\Phi = (2\pi/\lambda)\Delta nh$ also predicts a phase shift at 1064 nm approximately half that at 532 nm. A quantitative extension would require wavelength-dependent values of α_0, β, n_2, and dn/dT. In addition, the model represents porosity only through its volume fraction. Therefore, films with the same porosity but different pore sizes, packing, or spatial organization are considered equivalent. However, these structural features can modify light trapping, nanotube contacts, and thermal transport [45,46]. Structural defects can also modify optical transitions and reduce thermal conductivity [47], while catalyst particles, amorphous carbon, residual surfactants, and binders may alter the effective properties of the film; for example, surfactant removal has been shown to increase the electrical conductance of CNT films [48]. These effects are currently included only indirectly through literature-based effective properties. Future models could incorporate morphology- and composition-dependent coefficients, explicit three-dimensional pore structures, or multiphase descriptions, while time-dependent density functional theory could provide wavelength- and field-dependent optical parameters [49,50].

Finally, experimental validation of the predicted responses is needed to assess the scope and applicability of the results. Such validation would require a combination of structural, optical, thermal, and magneto-optical characterization techniques. Film thickness can be measured by cross-sectional scanning electron microscopy or profilometry, while

pore morphology and porosity can be evaluated using gas-adsorption BET analysis [51]. Nanotube alignment can be quantified by polarized Raman spectroscopy [52]. The effective optical transmittance and absorption coefficients can be obtaining used UV–Vis–NIR spectra measurements. Z-scan measurements could determine the nonlinear absorption and Kerr-like coefficients, while pump–probe experiments could separate the fast electronic contribution from the slower thermal response [53]. Finally, magneto-optical effects can be explored using ellipsometry under a controlled magnetic field to determine nonlinear properties [54]. Applying these techniques to films with equivalent architectures and excitation conditions would allow direct validation of the predicted trends and absolute values.

4. Conclusions

A multiphysics framework was developed to determine how thickness, porosity, and nanotube alignment jointly control the optical, thermal, and magneto-optical responses of MWCNT films. The results show that these structural parameters affect each response differently, so no single configuration maximizes all the evaluated behaviors. The thin and porous F3 and F4 configurations produce the highest and closely comparable temperature rises and refractive-index changes because of their low areal heat capacity. F3 shows a slightly greater response because its random nanotube network limits lateral heat transport, whereas the partial alignment in F4 increases both optical coupling and heat spreading. Conversely, the thicker F11 configuration produces the largest accumulated phase-shift magnitude because of its longer optical interaction length. Under nanosecond excitation, heat accumulation makes the thermo-optic contribution dominant. As the pulse duration decreases toward the picosecond regime at fixed peak irradiance and repetition rate, the deposited energy and photothermal effect decreases. Consequently, the electronic Kerr-like and magneto-optical contributions account for a larger fraction of the total refractive-index response. Thus, the model identifies architecture- and pulse-dependent trends that provide testable predictions for future experimental studies of tunable coatings, optical modulators, and photothermal or magnetic sensing devices.

Funding: The author thanks ANID for FONDECYT Iniciación project N°11250606.

Data Availability Statement: Data are not available for sensibility.

Acknowledgments: During the preparation of this work, the author used ChatGPT-5.6 Plus to improve the English language, to refine the redaction, and to refine the Figure 1 and graphical abstract. After using this tool/service, the author reviewed and edited the content as needed and took full responsibility for the content of the published article.

Conflicts of Interest: The author declares no conflict of interest.

References

1. Komori, T.; Tamai, R.; Nakazawa, Y.; Hoshino, K.; Abe, H.; Tanaka, S.; Takashiri, M. Stable Photothermal Conversion in Single-Walled Carbon Nanotube Device with Pn-Junction under Uniform Sunlight Irradiation. *Mater. Today Commun.* **2024**, *38*, 108436. [CrossRef]
2. Crank, B.; Fricker, B.; Hubbard, A.; Hitawala, H.; Muna, F.I.; Okunlola, O.S.; Doherty, A.; Hulteen, A.; Powers, L.; Purtell, G.; et al. Electromagnetic Radiation Shielding Using Carbon Nanotube and Nanoparticle Composites. *Appl. Sci.* **2025**, *15*, 8696. [CrossRef]
3. Sun, T.; Yang, J.; Kang, F.; Zhang, W.; Hui, J.; Li, X.; Zhang, Q. CNT-Based Electrodes for Flexible Aqueous Zinc-Ion Batteries: Progress and Opportunities. *Mater. Chem. Front.* **2025**, *9*, 2844–2862. [CrossRef]
4. Zeng, Z.; Wang, G.; Wolan, B.F.; Wu, N.; Wang, C.; Zhao, S.; Yue, S.; Li, B.; He, W.; Liu, J.; et al. Printable Aligned Single-Walled Carbon Nanotube Film with Outstanding Thermal Conductivity and Electromagnetic Interference Shielding Performance. *Nanomicro Lett.* **2022**, *14*, 179. [CrossRef]
5. Zhang, M.; Ban, D.; Xu, C.; Yeow, J.T.W. Large-Area and Broadband Thermoelectric Infrared Detection in a Carbon Nanotube Black-Body Absorber. *ACS Nano* **2019**, *13*, 13285–13292. [CrossRef]

6. Chawla, K.; Cai, J.; Thompson, D.; Thevamaran, R. Superior Thermal Transport Properties of Vertically Aligned Carbon Nanotubes Tailored through Mesoscale Architectures. *Carbon* **2024**, *216*, 118526. [CrossRef]
7. Li, Z.; Bai, B.; Li, C.; Dai, Q. Efficient Photo-Thermionic Emission from Carbon Nanotube Arrays. *Carbon* **2016**, *96*, 641–646. [CrossRef]
8. Martines-Arano, H.; Barmavatu, P.; Abdul Jameel, A.G.; Carreto-Hernandez, L.G.; Mercado-Zúñiga, C.; Hevia, S.; García-Merino, J.A. Photothermal Emissivity of Carbon Nanotubes Coatings for Enhanced Thermal Waste Management. *J. Quant. Spectrosc. Radiat. Transf.* **2025**, *342*, 109488. [CrossRef]
9. Huang, Y.; Yang, K.; Gao, J.; Zhao, Z.; Li, H.; Wang, Z. Study on the Law and Mechanism of Anisotropic Conductivity of Carbon Nanotubes Film Prepared by Floating Catalytic Chemical Vapor Deposition Method. *J. Mater. Res. Technol.* **2023**, *26*, 3571–3585. [CrossRef]
10. Begzaad, S.; Happe, E.D.; Gouws, G.; Plank, N.O.V. AFM Analysis of Morphology–Density–Transport Relationships in Carbon Nanotube Thin Films. *Nanotechnology* **2026**, *37*, 245201. [CrossRef]
11. Conley, K.; Karttunen, A.J. Bridging the Junction: Electrical Conductivity of Carbon Nanotube Networks. *J. Phys. Chem. C* **2022**, *126*, 17266–17274. [CrossRef]
12. Kumanek, B.; Janas, D. Thermal Conductivity of Carbon Nanotube Networks: A Review. *J. Mater. Sci.* **2019**, *54*, 7397–7427. [CrossRef]
13. Walker, J.S.; Macdermid, Z.J.; Fagan, J.A.; Kolmakov, A.; Biacchi, A.J.; Searles, T.A.; Walker, A.R.H.; Rice, W.D. Dependence of Single-Wall Carbon Nanotube Alignment on the Filter Membrane Interface in Slow Vacuum Filtration. *Small* **2022**, *18*, 2105619. [CrossRef]
14. Wang, Y.; Duan, G.; Zhang, L.; Ma, L.; Zhao, X.; Zhang, X. Terahertz Dispersion Characteristics of Super-Aligned Multi-Walled Carbon Nanotubes and Enhanced Transmission through Subwavelength Apertures. *Sci. Rep.* **2018**, *8*, 2087. [CrossRef]
15. Licht, G.; Licht, S. Carbon Nanotube Production Pathways: A Review of Chemical Vapor Deposition and Electrochemical CO2 Conversion, Such as C2CNT. *Crystals* **2025**, *15*, 887. [CrossRef]
16. Pant, M.; Singh, R.; Negi, P.; Tiwari, K.; Singh, Y. A Comprehensive Review on Carbon Nano-Tube Synthesis Using Chemical Vapor Deposition. *Mater. Today Proc.* **2021**, *46*, 11250–11253. [CrossRef]
17. Vir Singh, M.; Kumar Tiwari, A.; Gupta, R. Catalytic Chemical Vapor Deposition Methodology for Carbon Nanotubes Synthesis. *ChemistrySelect* **2023**, *8*, e202204715. [CrossRef]
18. An, L.; Friedrich, C. Dielectrophoretic Assembly of Carbon Nanotubes and Stability Analysis. *Prog. Nat. Sci. Mater. Int.* **2013**, *23*, 367–373. [CrossRef]
19. Kim, D.Y.; Kim, J.H.; Li, M.; Noda, S.; Kim, J.; Kim, K.-S.; Kim, K.S.; Yang, C.-M. Controllable Pore Structures of Pure and Sub-Millimeter-Long Carbon Nanotubes. *Appl. Surf. Sci.* **2021**, *566*, 150751. [CrossRef]
20. He, X.; Gao, W.; Xie, L.; Li, B.; Zhang, Q.; Lei, S.; Robinson, J.M.; Hároz, E.H.; Doorn, S.K.; Wang, W.; et al. Wafer-Scale Monodomain Films of Spontaneously Aligned Single-Walled Carbon Nanotubes. *Nat. Nanotechnol.* **2016**, *11*, 633–638. [CrossRef]
21. Wang, B.; Banerjee, S.; Zhang, P. Statistical Analysis of Intertube Tunneling Contacts in the Macroscopic Electrical Conductivity of Carbon Nanotube Fibers. *ACS Appl. Electron. Mater.* **2025**, *7*, 1192–1201. [CrossRef]
22. Qiu, L.; Wang, X.; Tang, D.; Zheng, X.; Norris, P.M.; Wen, D.; Zhao, J.; Zhang, X.; Li, Q. Functionalization and Densification of Inter-Bundle Interfaces for Improvement in Electrical and Thermal Transport of Carbon Nanotube Fibers. *Carbon* **2016**, *105*, 248–259. [CrossRef]
23. Lee, S.; Baek, S.; Park, C.; Shin, D.; Kim, J.; Sung, Y. Experimental Study on the Porous Structure and Heat Dissipation Characteristics of Multiwalled Carbon Nanotube Films with Added Cellulose Nanocrystals. *Case Stud. Therm. Eng.* **2025**, *67*, 105814. [CrossRef]
24. García-Merino, J.A. Morphological Effects on the Photothermal Properties and Photo-Thermionic Emission in Carbon Nanotubes. *J. Mod. Opt.* **2024**, *71*, 427–438. [CrossRef]
25. García-Merino, J.A.; Martínez-González, C.L.; San Miguel, C.R.T.; Trejo-Valdez, M.; Martínez-Gutiérrez, H.; Torres-Torres, C. Magneto-Conductivity and Magnetically-Controlled Nonlinear Optical Transmittance in Multi-Wall Carbon Nanotubes. *Opt. Express* **2016**, *24*, 19552. [CrossRef]
26. García-Merino, J.A.; Mercado-Zúñiga, C.; Martínez-González, C.L.; Torres-SanMiguel, C.R.; Vargas-García, J.R.; Torres-Torres, C. Magneto-Conductive Encryption Assisted by Third-Order Nonlinear Optical Effects in Carbon/Metal Nanohybrids. *Mater. Res. Express* **2017**, *4*, 035601. [CrossRef]
27. Lopez-Bastida, A.; Mercado-Zúñiga, C.; Bornacelli, J.; de la Rosa, J.M.; Torres-Torres, C. All-Optical Encryption Controlled by Multiphotonic Absorption in Carbon Nanotubes. *Photonics* **2024**, *11*, 1029. [CrossRef]
28. Xia, F.; Xia, T.; Su, H.; Gan, L.; Hu, Q.; Wang, W.; Huang, R.; Bai, T.; Chen, Y.; Ma, C.; et al. Flexible Radio-Frequency Carbon Nanotube Transistors Operating at Frequencies above 100 GHz. *Nat. Electron.* **2026**, *9*, 788–796. [CrossRef]

29. Bulmer, J.S.; Lekawa-Raus, A.; Rickel, D.G.; Balakirev, F.F.; Koziol, K.K. Extreme Magneto-Transport of Bulk Carbon Nanotubes in Sorted Electronic Concentrations and Aligned High Performance Fiber. *Sci. Rep.* **2017**, *7*, 12193. [CrossRef]
30. Mercado-Zúñiga, C.; Oliva, J.; Vargas-García, J.R.; Diaz-Torres, L.A.; Gomez-Solis, C. Effect of Pt Loading on the Hydrogen Production of CNT/Pt Composites Functionalized with Carboxylic Groups. *Int. J. Hydrogen Energy* **2020**, *45*, 27012–27025. [CrossRef]
31. Hernández-Acosta, M.A.; Martínez-González, C.L.; Torres-SanMiguel, C.R.; Trejo-Valdez, M.; Martínez-Gutiérrez, H.; Torres-Torres, C. Electronically Controlled Optical Polarization Evolution in Carbon Nanotubes. *Math. Methods Appl. Sci.* **2026**, *49*, 7497–7506. [CrossRef]
32. García-Merino, J.A.; Jiménez-Marín, E.; Mercado-Zúñiga, C.; Trejo-Valdez, M.; Vargas-García, J.R.; Torres-Torres, C. Quantum and Bistable Magneto-Conductive Signatures in Multiwall Carbon Nanotubes Decorated with Bimetallic Ni and Pt Nanoparticles Driven by Phonons. *OSA Contin.* **2019**, *2*, 1285. [CrossRef]
33. Wang, D.; Song, P.; Liu, C.; Wu, W.; Fan, S. Highly Oriented Carbon Nanotube Papers Made of Aligned Carbon Nanotubes. *Nanotechnology* **2008**, *19*, 075609. [CrossRef]
34. Xia, X.; Zhou, S.; Wang, Y.; Zhang, Z. Emerging Optoelectronic Architectures in Carbon Nanotube Photodetector Technologies. *Fundam. Res.* **2025**, *5*, 1153–1168. [CrossRef]
35. Wąsik, M.; Dużyńska, A.; Judek, J.; Pawłowski, M.; Świtkowski, K.; Witowski, A.M.; Zdrojek, M. Ultraviolet to Far-Infrared Transmission Properties of Thin Film Multi-Walled Carbon Nanotube Random Networks. *J. Mater. Sci.* **2017**, *52*, 3086–3094. [CrossRef]
36. Yu, X.; Rajamani, R.; Stelson, K.A.; Cui, T. Carbon Nanotube Based Transparent Conductive Thin Films. *J. Nanosci. Nanotechnol.* **2006**, *6*, 1939–1944. [CrossRef]
37. Ovsiienko, I.V.; Len, T.A.; Mirzoiev, I.G.; Beliayev, E.Y.; Gnida, D.; Matzui, L.Y.; Heraskevych, V.M. Low-Temperature Magnetoresistance of Multi-Walled Carbon Nanotubes with Perfect Structure. *Low Temp. Phys.* **2022**, *48*, 89–98. [CrossRef]
38. García-Merino, J.A.; Villarroel, R.; Mercado-Zúñiga, C.; Morales-Bonilla, S. Coatings Based on Hybrid Carbon-Platinum Nano-Ink for Multifunctional Applications. *J. Alloys Compd.* **2025**, *1022*, 180132. [CrossRef]
39. Vinetsky, Y.; Jambu, J.; Mandler, D.; Magdassi, S. CNT-Based Solar Thermal Coatings: Absorptance vs. Emittance. *Coatings* **2020**, *10*, 1101. [CrossRef]
40. García-Merino, J.A.; Fernández-Izquierdo, L.; Villarroel, R.; Hevia, S.A. Photo-Thermionic Emission and Photocurrent Dynamics in Low Crystallinity Carbon Nanotubes. *J. Mater.* **2021**, *7*, 271–280. [CrossRef]
41. Villarroel, R.; Martines-Arano, H.; Chávez-Ángel, E.; Hevia, S.; García-Merino, J.A. Enhanced Thermionic Emission from Annealed CNT Cathodes Assessed via Chaos-Based Electrical Diagnostics. *Synth. Met.* **2026**, *318*, 118111. [CrossRef]
42. García-Merino, J.A.; Martínez-González, C.L.; Miguel, C.R.T.-S.; Trejo-Valdez, M.; Martínez-Gutiérrez, H.; Torres-Torres, C. Photothermal, Photoconductive and Nonlinear Optical Effects Induced by Nanosecond Pulse Irradiation in Multi-Wall Carbon Nanotubes. *Mater. Sci. Eng. B* **2015**, *194*, 27–33. [CrossRef]
43. Kaniyoor, A.; Gspann, T.S.; Mizen, J.E.; Elliott, J.A. Quantifying Alignment in Carbon Nanotube Yarns and Similar Two-dimensional Anisotropic Systems. *J. Appl. Polym. Sci.* **2021**, *138*, 50939. [CrossRef]
44. Soncini, A.; Fowler, P.W. Non-Linear Ring Currents: Effect of Strong Magnetic Fields on π-Electron Circulation. *Chem. Phys. Lett.* **2004**, *400*, 213–220. [CrossRef]
45. Gspann, T.S.; Juckes, S.M.; Niven, J.F.; Johnson, M.B.; Elliott, J.A.; White, M.A.; Windle, A.H. High Thermal Conductivities of Carbon Nanotube Films and Micro-Fibres and Their Dependence on Morphology. *Carbon* **2017**, *114*, 160–168. [CrossRef]
46. Ghai, V.; Singh, H.; Agnihotri, P.K. Structure Dependent Broadband Optical Absorption in Carbon Nanotubes. *ACS Appl. Opt. Mater.* **2023**, *1*, 252–260. [CrossRef]
47. Harutyunyan, H.; Gokus, T.; Green, A.A.; Hersam, M.C.; Allegrini, M.; Hartschuh, A. Defect-Induced Photoluminescence from Dark Excitonic States in Individual Single-Walled Carbon Nanotubes. *Nano Lett.* **2009**, *9*, 2010–2014. [CrossRef]
48. Wang, J.; Sun, J.; Gao, L.; Wang, Y.; Zhang, J.; Kajiura, H.; Li, Y.; Noda, K. Removal of the Residual Surfactants in Transparent and Conductive Single-Walled Carbon Nanotube Films. *J. Phys. Chem. C* **2009**, *113*, 17685–17690. [CrossRef]
49. Preciado-Rivas, M.R.; Torres-Sánchez, V.A.; Mowbray, D.J. Optical Absorption and Energy Loss Spectroscopy of Single-Walled Carbon Nanotubes. *Phys. Rev. B* **2019**, *100*, 235429. [CrossRef]
50. Oliveira, M.J.T.; Medeiros, P.V.C.; Sousa, J.R.F.; Nogueira, F.; Gueorguiev, G.K. Optical and Magnetic Excitations of Metal-Encapsulating Si Cages: A Systematic Study by Time-Dependent Density Functional Theory. *J. Phys. Chem. C* **2014**, *118*, 11377–11384. [CrossRef]
51. Papia, E.-M.; Kondi, A.; Singh, V.; Tiwari, M.K.; Gogolides, E.; Constantoudis, V. SEM-Based Analysis of Pore Uniformity: Effects of Pore Positions and Sizes. *Mater. Today Commun.* **2026**, *53*, 115342. [CrossRef]
52. Banihashemian, S.M.; Mesbah, M.; Kamyab, H.; Taheri, M.M.; Balasubramanian, B. Polarized Raman Spectroscopy of Aligned DNA-Wrapped Single-Wall Carbon Nanotubes. *Carbon Trends* **2025**, *19*, 100469. [CrossRef]

53. Vanyukov, V.V.; Shuba, M.V.; Nasibulin, A.G.; Svirko, Y.P.; Kuzhir, P.P.; Mikheev, G.M. Saturable Absorption and Nonlinear Refraction in Free-Standing Carbon Nanotube Film: Theory and Experiment. *Carbon* **2022**, *186*, 509–519. [CrossRef]
54. Zhu, S.; Zhang, H.; Martín Valderrama, C.; Bravo, L.; Wang, X.; Song, B.; Berger, A. Generalized Magneto-Optical Ellipsometry in the Presence of Strong Second-Order Magneto-Optical Effects. *J. Phys. D Appl. Phys.* **2026**, *59*, 315003. [CrossRef]

Disclaimer/Publisher's Note: The statements, opinions and data contained in all publications are solely those of the individual author(s) and contributor(s) and not of MDPI and/or the editor(s). MDPI and/or the editor(s) disclaim responsibility for any injury to people or property resulting from any ideas, methods, instructions or products referred to in the content.